

Analysis of Interactions Among Parallel Grid-Forming Inverters

T. Thilekha, S. Filizadeh, U. D. Annakkage, C. Karawita, D. Muthumuni

Abstract—Parallel operation of grid-forming inverters (GFMI) is often achieved using droop characteristics implemented in converter controllers. Converters' recovery after a disturbance depends on the dynamics of each individual GFMI, and the droop characteristic alone is unable to ensure successful parallel operation. This work proposes a dynamic-phasor based modeling approach that enables eigenvalue analysis of multi-converter systems to identify the underlying factors that affect the interactions among parallel GFMI. Network dynamics are included through dynamic phasor modeling of its elements, and controller dynamics are fully included. Modeling modularity is preserved, which allows to easily extend the test system to any topology of interest. The results presented for an exemplar two-converter system prove that the virtual inertia time-constant plays a significant role in exciting interactions, and that network and control system parameters are vital in extending the stability margins of the systems. EMT simulation results from PSCAD/EMTDC are included to verify the validity of the predictions of the dynamic-phasor based model.

Keywords—Eigenvalue analysis, grid-forming inverters, inertia, interactions, parallel operation.

I. INTRODUCTION

TECHNOLOGICAL advances in power electronics and control methods have led to large-scale adoption of grid-tied inverters for the connection of renewable generation resources and energy storage devices. Replacing conventional generation units with inverter-based resources deteriorates the inertia and strength of the grid that would, otherwise, have been provided by synchronous machines (SMs). Advanced inverter control techniques have been suggested to address these issues [1], [2], including emulation of synchronous machine characteristics, commonly known as virtual synchronous machine (VSM) methods. Depending on the order of the emulated SM, a number of VSM methods are suggested [1], [2]. Active power-frequency (P - f) droop and reactive power-voltage (Q - v) droop characteristics are commonly found in VSM topologies and provide primary frequency and voltage regulation functionalities, respectively. To emulate the inertial characteristics of a SM, the dynamics

of its swing equation may be incorporated in the P - f controller. An inverter operating with such control abilities is often termed a grid-forming inverter (GFMI) and presents as a controlled voltage source to the grid.

Due to the low thermal capability of power electronic switches [2], current-limiting algorithms have to be incorporated into grid-forming control methods. There are a number of current-limiting algorithms in the literature [2], [3], including the virtual-impedance-based current limiter that allows the GFMI to continue to operate as a voltage source when current-limiting is invoked. This paper uses a current-dependent virtual-impedance method [3] to reduce the inrush current following large disturbances.

Although the droop controller enables parallel operation of GFMI, it does not guarantee parallel operation at all times. Poorly selected controller parameters and network conditions may easily lead to sustained or growing oscillations. Frequency-domain models have been developed for single GFMI for parameter selection [4]; however, extending their conclusions is invalid for parallel-connected GFMI as such systems are prone to interactions. In a few references, active power oscillations have been observed in parallel-connected GFMI [5]–[7]. These oscillations have been reduced by introducing more damping to the system via controller modifications. The impact of inertia in exciting post-disturbance oscillations is explained in [5], but it has ignored the network dynamics by modeling the network using constant admittances. The root causes of interactions in multi-inverter systems are not fully known and various network and control parameters lead to the excitation of critical modes in the system. This paper addresses this critical problem by conducting an eigenvalue-based analysis of a system that includes all the control and network dynamics.

Impedance-based [8] and eigenvalue-based methods are commonly used to analyze the stability margins of inverters [7]. Eigenvalue-based analysis is more attractive in power system applications due to its ability to identify the states that significantly participate in the oscillatory mode(s) [9]. This paper uses small-signal modeling [10], [11], wherein each paralleled inverter is modeled in its own reference frame; one of the reference frames is then selected as the common reference frame. Relevant variables are transformed to and from the common reference frame using proper transformation matrices. This modeling method preserves modularity, which enables the addition or removal of any dynamic device. An eigenvalue-based analysis is then conducted to identify critical modes. Participation factors of the critical modes are calculated to identify major participating state variables.

This work was supported in part by Mitacs, Manitoba HVDC Research Center, and Natural Sciences and Engineering Research Council (NSERC) of Canada.

T. Thilekha, S. Filizadeh, and U. D. Annakkage are with the Department of Electrical and Computer Engineering, University of Manitoba, Winnipeg, Canada (e-mail: muthukut@myumanitoba.ca | shaahin.filizadeh@umanitoba.ca | udaya.annakkage@umanitoba.ca). C. Karawita is with Transgrid Solutions Inc., Winnipeg, Canada (e-mail:ckarawita@tgs.biz). D. Muthumuni is with Manitoba HVDC Research Center, Winnipeg, Canada (e-mail: dharshana@mhi.ca).

Paper submitted to the International Conference on Power Systems Transients (IPST2023) in Thessaloniki, Greece, June 12-15, 2023.

Control and network parameters that influence those states are changed to identify their sensitivity on the inverter interactions. This study gives a detailed analysis of the impact of the VSM controller and the network on post-disturbance oscillations in paralleled GFMI.

The main contributions of this study include:

- A small-signal modeling approach is applied to the adopted grid-forming controller with P - f control, Q - v control, and transient virtual impedance path.
- This study shows that interactions can happen even between GFMI with identical control and network parameters.
- The possibility of expanding the stable region of operation without introducing additional damping paths and merely by properly matching the dynamics of P - f and Q - v controller paths has been demonstrated.

The rest of the paper is arranged as follows. Section II explains the test system, the controller topology, and the small-signal modeling of the test system. The eigenvalue analysis and results are given in Section III. Conclusions are given in Section IV.

II. DESCRIPTION AND MODELING OF THE TEST SYSTEM

In the system shown in Fig. 1, two grid-forming voltage source converters are connected to the same point of interconnection (POI) using LC filters, step-up transformers, and 10 km long transmission lines. As shown in Fig. 2, the grid-forming controller consists of an active power-frequency (P - f) controller, reactive power-voltage (Q - v) controller and virtual-impedance (VI) based current controller path. The (P - f) droop and swing equation-based P - f controller and (Q - v) droop-based Q - v controller are given in Figs. 3 and 4, respectively. The VI-based controller in Fig. 5 consists of the current-dependent VI path and transient VI paths.

The current dependent VI path will activate only if the converter current (i_{cvrms}) exceeds the set current threshold ($i_{threshold}$) value. R_{vi} is the virtual resistance proportional to this current difference. The dq components of the converter current are multiplied by R_{vi} . This action mimics a virtual voltage drop between the converter terminal and filter inductance (L_f). The transient VI path activates following the transients in the converter current and, therefore, acts as an active damping path to the converter currents. In the transient VI path, a constant virtual resistance value (R_{vi0}) is multiplied by the high-frequency components of the converter currents' dq components. This path also emulates a voltage drop between the converter terminal and the filter inductance. These two VI paths provide transient virtual voltage drops to control the converter current, given that the criterion to activate each path is met. The continuous control of the grid-forming inverter's terminal voltage is carried out through Q - v droop-based PI controller. Tables I-II give the parameters that are used in the simulations of this test system in the paper.

In the development of the model, switching transients are ignored as their frequency lies above the frequency range of interest; dc-side dynamics are also excluded, although they can be easily augmented onto the model. Unlike conventional

TABLE I
TEST SYSTEM PARAMETERS

| | | |
|-------------------------------|-------------------------------|-----------------------------|
| $S_{rated} = 500$ kVA | $V_{dclink} = 820$ V | $L_f = 85$ μ H |
| $R_L = 172.8$ Ω | $L_L = 0.917$ H | $C_f = 828.9$ μ F |
| $L_{tf} = 0.1$ pu | $R_{tf} = 0.01$ pu | $R_f = 0.0755$ Ω |
| $R_{tx} = 0.103$ Ω /km | $X_{tx} = 0.405$ Ω /km | $Y_{tx} = 4.117$ μ S/km |

TABLE II
GRID-FORMING CONTROLLER PARAMETERS

| | | | |
|--------------------------|-------------------|------------------|-------------------------|
| $H = 3$ s | $T_p = 0.001$ s | $D_p = 0.03$ pu | $P_{ref} = 0.7$ pu |
| $T_v = 0.001$ s | $T_q = 0.001$ s | $D_q = 0.03$ pu | $Q_{ref} = 0.35$ pu |
| $K_p = 0.1$ pu | $T_i = 0.25$ s | $f_0 = 60$ Hz | $\omega_{ref} = 1.0$ pu |
| $R_{vi0} = 0.25$ | $f_{hp} = 0.5$ Hz | $f_{sw} = 4$ kHz | $E_{ref} = 1.0$ pu |
| $i_{threshold} = 1.1$ pu | | $K_{PRVI} = 5$ | |

synchronous-machine dominated power systems, the short response time of an inverter may lead to interactions with the network [10]. Therefore, the developed model includes the dynamics of the network using dynamic phasor representation of network elements.

This paper uses ‘‘Component Connection Method’’ [11] to develop the small-signal model (SSM). Here the power system is decomposed into its subcomponents (e.g., grid-forming and grid-following inverters, synchronous machines, filters, π -sections etc.) and each subcomponent is linearized locally to obtain its linear, time-invariant model. Then these component models are interconnected by linear algebraic relationships defined by their input-output variables. The linear algebraic interconnection of these components reduces the computational effort greatly, compared with a generic state-space model [11]. The block diagram in Fig. 6 provides a visual representation of how the method used in this study may be used to develop models for systems comprising a large number of network components and grid-forming inverters. In this figure, the GFMI- i block represents any GFM controller topology with the average-value model of the inverter as well as its converter controller. Dynamic devices are not limited to grid-forming inverters and may include any dynamic device, e.g., synchronous machines, grid-following inverters, etc.

In developing the small-signal model, the system in Fig. 1 is divided into four sub-sections: the control system (bordered in red), LC filter and transformer (bordered in blue), network (bordered in green), and load (bordered in orange). The first three sub-sections for each inverter are modeled using an individual reference frame whose rotational speed is governed by the inverter's own P - f controller. The reference frame of one of the GFMI is selected as the common reference frame, which is also used to model the load dynamics. The transformation angle (δ_i) is obtained as shown in Fig. 7, where ($D - Q$) represents the common reference frame rotating at ω_{com} , and ($d_i - q_i$) represents the i^{th} inverter's reference frame, which rotates at ω_i . The direction of the transformation angle is modified from [10] to match the Park's transformation matrix used in this work. To obtain the overall small-signal model, relevant state variables are transformed to and from the common reference frame. The variables in each individual inverter reference frame can be transformed into the common reference frame as in (1) using the transformation matrix $[T_i]$

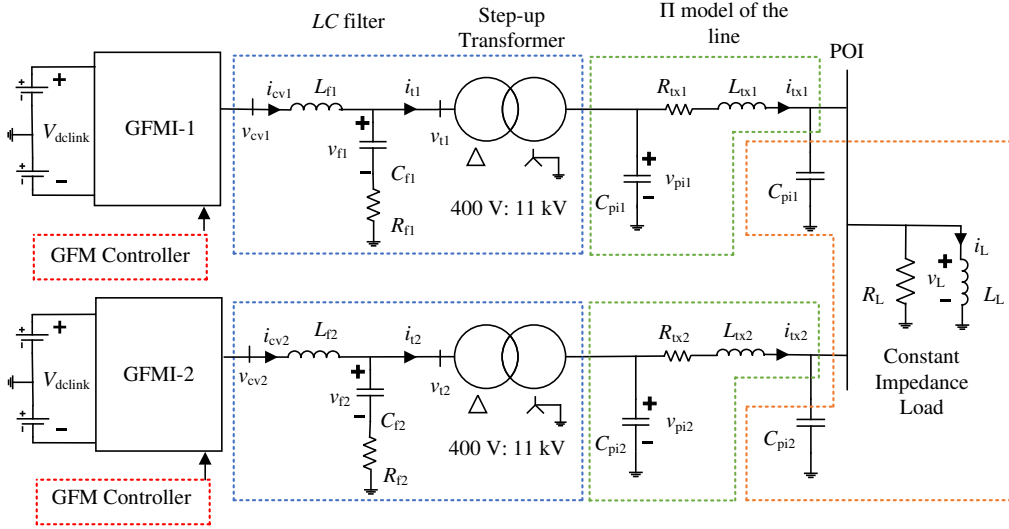


Fig. 1. Schematic diagram of the test system.

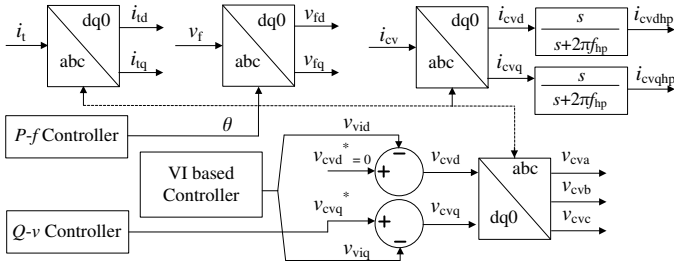


Fig. 2. Block diagram of the grid-forming controller.

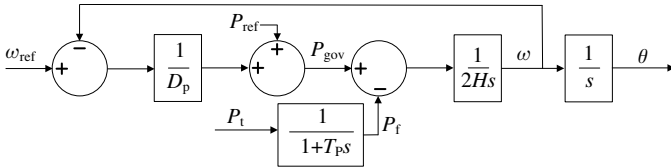


Fig. 3. Block diagram of the P - f controller.

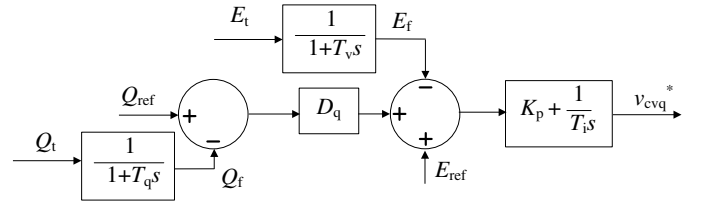


Fig. 4. Block diagram of the Q - v controller.

Fig. 3. Block diagram of the P - f controller.

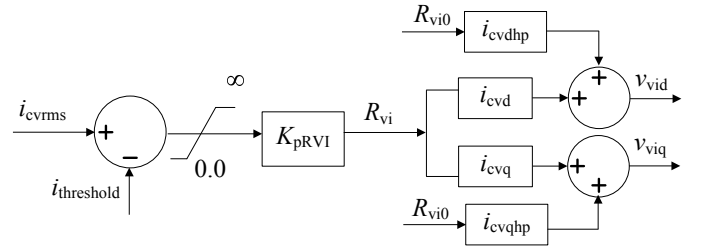


Fig. 5. Block diagram of the VI controller.

given in (2). The corresponding inverse transformation, $[T_i]^{-1}$, is given in (3). The small-signal model for each sub-section is described next.

$$[x_{DQ}] = [T_i] [x_{dq}] \quad (1)$$

$$[T_i] = \begin{bmatrix} \cos(\delta_i) & -\sin(\delta_i) \\ \sin(\delta_i) & \cos(\delta_i) \end{bmatrix} \quad (2)$$

$$[T_i]^{-1} = \begin{bmatrix} \cos(\delta_i) & \sin(\delta_i) \\ -\sin(\delta_i) & \cos(\delta_i) \end{bmatrix} \quad (3)$$

A. Power Controller

The power controller consists of P - f and Q - v paths. The inverter's output active power, P_t , and reactive power, Q_t , are calculated at the terminals of the LC filter of each inverter. The dynamics of the proportional-integral (PI) controller in the Q - v control loop is modeled by the state variable x_1 . The

resulting set of non-linear equations that describes the power controllers is given by (4)-(9).

$$d\delta/dt = \omega_{com} - \omega \quad (4)$$

$$d\omega/dt = -P_t/2H - \omega/2HD_p + 1/2H(P_{ref} + \omega_{ref}/D_p) \quad (5)$$

$$dP_f/dt = -P_f/T_p + P_t/T_p \quad (6)$$

$$dQ_f/dt = -Q_f/T_q + Q_t/T_q \quad (7)$$

$$dE_f/dt = -E_f/T_v + E_t/T_v \quad (8)$$

$$dx_1/dt = D_q(Q_{ref} - Q_f) + E_{ref} - E_f \quad (9)$$

where

$$P_t = [v_{fd} + (i_{cvd} - i_{td})R_f]i_{td} + [v_{fq} + (i_{cvq} - i_{tq})R_f]i_{tq}$$

$$Q_t = -[v_{fq} + (i_{cvq} - i_{tq})R_f]i_{td} + [v_{fd} + (i_{cvd} - i_{td})R_f]i_{tq}$$

$$E_t = [[v_{fd} + (i_{cvd} - i_{td})R_f]^2 + [v_{fq} + (i_{cvq} - i_{tq})R_f]^2]^{1/2}$$

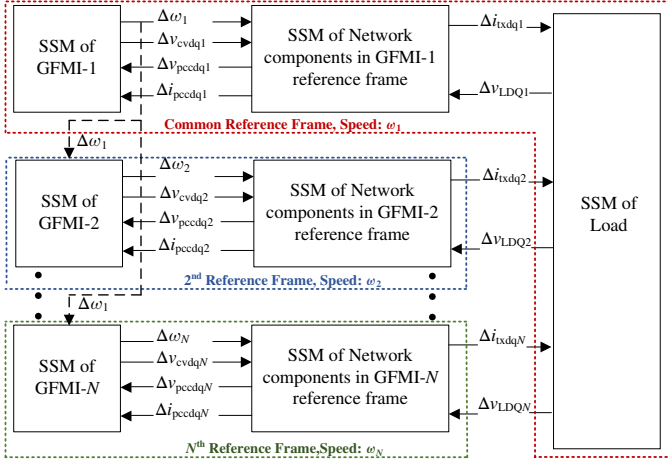


Fig. 6. The block diagram representation of the adopted small-signal model development procedure.

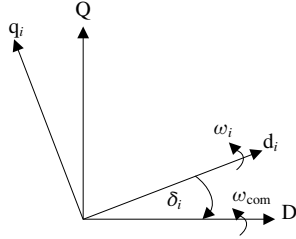


Fig. 7. Individual and common reference frames.

The state equations in (10) are obtained after linearizing (4)-(9).

$$\begin{aligned} [\Delta \dot{X}_P] &= [A_{Pd1}] [\Delta X_P] + [A_{Pd2}] [\Delta X_{LCL}] \\ &+ [A_{Pd3}] [\Delta X_N] + [A_{Pd4}] [\Delta X_L] + [B_{Pd}] [\Delta U_{inv}] \end{aligned} \quad (10)$$

The Q - v controller's output, v_{cvq}^* , is given by (11) and is linearized as in (12).

$$v_{cvq}^* = K_P(D_q(Q_{ref} - Q_f) + E_{ref} - E_f) + x_1/T_i \quad (11)$$

$$[\Delta v_{cvq}^*] = [C_{Pd}] [\Delta X_P] + [D_{Pd}] [\Delta U_{inv}] \quad (12)$$

where

$$[\Delta X_P] = [\Delta \delta \quad \Delta \omega \quad \Delta P_f \quad \Delta Q_f \quad \Delta E_f \quad \Delta x_1]^T$$

$$[\Delta X_{LCL}] = \begin{bmatrix} \Delta i_{cvd} & \Delta i_{cvq} & \Delta v_{fd} & \Delta v_{fq} & \Delta i_{td} & \Delta i_{tq} \dots \\ \dots & \Delta i_{cvdhp} & \Delta i_{cvqhp} & & & \end{bmatrix}^T$$

$$[\Delta X_N] = [\Delta v_{pid} \quad \Delta v_{piq} \quad \Delta i_{txd} \quad \Delta i_{txq}]^T$$

$$[\Delta X_L] = [\Delta v_{LD} \quad \Delta v_{LQ} \quad \Delta i_{LD} \quad \Delta i_{LQ}]^T$$

$$[\Delta U_{inv}] = [\Delta \omega_{ref} \quad \Delta P_{ref} \quad \Delta Q_{ref} \quad \Delta E_{ref}]^T$$

The expanded forms of the matrices in (10)-(12) can be readily derived, but are not shown due to space limitations.

B. LC Filter

The dynamics of the LC filter and the transformer are included as explained in this section. High-frequency converter current components, which are introduced by the transient VI-based current controller, are included in this section for convenience. In this study the converter is operated below $i_{threshold}$; therefore, the dynamics of the current-dependent VI path are excluded. The dq domain non-linear equations that govern the dynamics of the considered subgroup are given in (13) to (20).

$$di_{cvd}/dt = (R_f(i_{td} - i_{cvd}) - \omega L_f i_{cvq} + v_{cvd} - v_{fd})/L_f \quad (13)$$

$$di_{cvq}/dt = (R_f(i_{tq} - i_{cvq}) + \omega L_f i_{cvd} + v_{cvq} - v_{fq})/L_f \quad (14)$$

$$dv_{fd}/dt = (-\omega C_f v_{fq} - i_{td} + i_{cvd})/C_f \quad (15)$$

$$dv_{fq}/dt = (\omega C_f v_{fd} - i_{tq} + i_{cvq})/C_f \quad (16)$$

$$di_{td}/dt = -(R_f + R_t)i_{td} + R_f i_{cvd} - \omega L_t i_{tq} + v_{fd} - v_{pid})/L_t \quad (17)$$

$$di_{tq}/dt = -(R_f + R_t)i_{tq} + R_f i_{cvq} + \omega L_t i_{td} + v_{fq} - v_{piq})/L_t \quad (18)$$

$$di_{cvdhp}/dt = -i_{cvdhp}/T_{hp} + di_{cvd}/dt \quad (19)$$

$$di_{cvqhp}/dt = -i_{cvqhp}/T_{hp} + di_{cvq}/dt \quad (20)$$

where $T_{hp} = 1/2\pi f_{hp}$. Linearization of (13) - (20) results in (21).

$$\begin{aligned} [\Delta \dot{X}_{LCL}] &= [A_{LCL}] [\Delta X_{LCL}] + [B_{LCL1}] \Delta \omega + \\ &[B_{LCL2}] \begin{bmatrix} \Delta v_{cvd} \\ \Delta v_{cvq} \end{bmatrix} + [B_{LCL3}] \begin{bmatrix} \Delta v_{pid} \\ \Delta v_{piq} \end{bmatrix} + \end{aligned} \quad (21)$$

After accounting for the output of the Q - v controller and the transient VI path the relationships given in (22) and (23) are obtained for the expected dq components of the converter terminal voltage. Note that the transformer's winding configuration introduces a 30° phase shift, which is considered in these equations to refer all the low-voltage side quantities to the high-voltage side.

$$v_{cvd} = (v_{cvq}^*) \sin(30^\circ) - R_{vi0} i_{cvdhp} \quad (22)$$

$$v_{cvq} = (v_{cvq}^*) \cos(30^\circ) - R_{vi0} i_{cvqhp} \quad (23)$$

Linearizing (22) and (23) yields the following.

$$\begin{bmatrix} \Delta v_{cvd} \\ \Delta v_{cvq} \end{bmatrix} = \begin{bmatrix} E_{11} \\ E_{12} \end{bmatrix} [\Delta X_P] + \begin{bmatrix} E_{12} \\ E_{22} \end{bmatrix} [\Delta X_{LCL}] + \begin{bmatrix} F_1 \\ F_2 \end{bmatrix} [\Delta U_{inv}] \quad (24)$$

Substituting (24) in (21) yields (25). The expanded forms of the matrices in (25) are not shown for brevity.

$$\begin{aligned} [\Delta \dot{X}_{LCL}] &= [A_{LCLd1}] [\Delta X_P] + [A_{LCLd2}] [\Delta X_{LCL}] + \\ &[A_{LCLd3}] [\Delta X_N] + [A_{LCLd4}] [\Delta X_L] + [B_{LCLd}] [\Delta U_{inv}] \end{aligned} \quad (25)$$

C. Network

The inverter-side capacitor and the inductance of the π -section are considered in developing the dynamic equations in (26) - (29).

$$dv_{pid}/dt = -\omega v_{piq} + (i_{td} - i_{txd})/C_{pi} \quad (26)$$

$$dv_{piq}/dt = \omega v_{pid} + (i_{tq} - i_{txq})/C_{pi} \quad (27)$$

$$di_{txd}/dt = -\omega i_{txq} + (-R_{tx}i_{txd} + v_{pid} - v_{Ld})/L_{tx} \quad (28)$$

$$di_{txq}/dt = \omega i_{txd} + (-R_{tx}i_{txq} + v_{piq} - v_{Lq})/L_{tx} \quad (29)$$

where v_{Ld} and v_{Lq} are the d and q components of the load voltage after converting from the common reference frame to an individual reference frame as shown in (30).

$$\begin{bmatrix} v_{Ld} \\ v_{Lq} \end{bmatrix} = [T_i]^{-1} \begin{bmatrix} v_{LD} \\ v_{LQ} \end{bmatrix} \quad (30)$$

The equations in (31) are obtained after linearizing (26) - (29).

$$\begin{aligned} [\Delta \dot{X}_N] &= [A_N] [\Delta X_N] + [B_{N1}] [\Delta \omega] + \\ & [B_{N2}] \begin{bmatrix} \Delta i_{td} \\ \Delta i_{tq} \end{bmatrix} + [B_{N3}] \begin{bmatrix} \Delta v_{Ld} \\ \Delta v_{Lq} \end{bmatrix} \end{aligned} \quad (31)$$

The linearized form of (30) is given in (32).

$$\begin{bmatrix} \Delta v_{Ld} \\ \Delta v_{Lq} \end{bmatrix} = [T_{sd}] \begin{bmatrix} \Delta v_{LD} \\ \Delta v_{LQ} \end{bmatrix} + [T_{vd}] \Delta \delta \quad (32)$$

By substituting (32) in (31) the state equations of the network are obtained as follows.

$$\begin{aligned} [\Delta \dot{X}_N] &= [A_{Nd1}] [\Delta X_P] + [A_{Nd2}] [\Delta X_{LCL}] + \\ & [A_{Nd3}] [\Delta X_N] + [A_{Nd4}] [\Delta X_L] + [B_{Nd}] [\Delta U_{inv}] \end{aligned} \quad (33)$$

The above state equations are developed in individual inverter reference frames. Therefore, the overall state equations for the i^{th} inverter are obtained as follows.

$$\begin{aligned} [\Delta \dot{X}_{inv}]_i &= [A_{inv}]_i [\Delta X_{inv}]_i + [A_{invLoad}]_i [\Delta X_L] + \\ & [B_{inv}]_i [\Delta U_{inv}]_i \end{aligned} \quad (34)$$

where $[\Delta X_{inv}]_i = [\Delta X_P \ \Delta X_{LCL} \ \Delta X_N]^T$. The matrix that relates the states of the above-identified three sub-groups is given in (35).

$$[A_{inv}]_i = \begin{bmatrix} A_{Pd1} & A_{Pd2} & A_{Pd3} \\ A_{LCLd1} & A_{LCLd2} & A_{LCLd3} \\ A_{Nd1} & A_{Nd2} & A_{Nd3} \end{bmatrix} \quad (35)$$

The matrix given in (36) shows the relationship between the inverter states and the load states.

$$[A_{invLoad}]_i = [A_{Pd4} \ A_{LCLd4} \ A_{Nd4}]^T \quad (36)$$

The relationship between the inverter states to the inverter input matrix is described using (37).

$$[B_{inv}]_i = [B_{Pd} \ B_{LCLd} \ B_{Nd}]^T \quad (37)$$

The states of a particular inverter are independent of the states of other inverters, except for the transformation angle, (δ_i). Therefore, the relationship between the i^{th} inverter's states to

the states of the j^{th} inverter (not the common reference frame generator) is represented as follows.

$$[A_{inv}]_{i-j} = [0]_{18 \times 18} \quad (38)$$

The matrix ($[A_{inv}]_{i-com}$), which relates the states of the i^{th} inverter to the states of the inverter in the common reference frame, is the same as in (38), except the element that relates the common reference frame's rotational speed (ω_{com}) to the individual frame's transformation angle (δ_i) is equal to 1.

D. Load

The dynamics of the load-side capacitances of each transmission line and the load inductance are modeled in the common reference frame. The non-linear dynamic equations of this sub-group are given in (39)-(42). C_L is the total shunt capacitance and N is the number of parallel inverters. Current flows in the transmission lines are the inputs to this section. These current injections must be transformed from the corresponding individual reference frames to the common reference frame as shown in (43).

$$dv_{LD}/dt = -\omega_{com} v_{LQ} + (-v_{LD}/R_L - i_{LD} + \sum_{i=1}^N i_{txDi})/C_L \quad (39)$$

$$dv_{LQ}/dt = \omega_{com} v_{LD} + (-v_{LQ}/R_L - i_{LQ} + \sum_{i=1}^N i_{txQi})/C_L \quad (40)$$

$$di_{LD}/dt = -\omega_{com} i_{LQ} + v_{LD}/L_L \quad (41)$$

$$di_{LQ}/dt = \omega_{com} i_{LD} + v_{LQ}/L_L \quad (42)$$

$$\begin{bmatrix} i_{txDi} \\ i_{txQi} \end{bmatrix} = [T_i] \begin{bmatrix} i_{txdi} \\ i_{txqi} \end{bmatrix} \quad (43)$$

After linearization of (39) - (42) and (43) the state matrices given in (44) and (45) are obtained, respectively.

$$\begin{aligned} [\Delta \dot{X}_L] &= [A_L] [\Delta X_L] + [B_{L1}] \Delta \omega_{com} + \\ & [B_{L2}] \sum_{i=1}^N \begin{bmatrix} \Delta i_{txDi} \\ \Delta i_{txQi} \end{bmatrix} + [B_{L3}] \Delta R_L \end{aligned} \quad (44)$$

$$\begin{bmatrix} \Delta i_{txDi} \\ \Delta i_{txQi} \end{bmatrix} = [T_{sd}]^{-1} \begin{bmatrix} \Delta i_{txdi} \\ \Delta i_{txqi} \end{bmatrix} + [T_{id}] \Delta \delta \quad (45)$$

Substituting (45) in (44) yields:

$$\begin{aligned} [\Delta \dot{X}_L] &= \sum_{i=1}^N ([A_{Ld1i}] [\Delta X_{Pi}] + [A_{Ld2i}] [\Delta X_{LCLi}] + \\ & [A_{Ld3i}] [\Delta X_{Ni}]) + [A_{Load}] [\Delta X_L] + [B_{Load}] [\Delta R_L] \end{aligned} \quad (46)$$

Equation (46) may be rewritten in a simplified form as in (47).

$$\begin{aligned} [\Delta \dot{X}_L] &= \sum_{i=1}^N ([A_{Loadinv}]_i [\Delta X_{inv}]_i) + \\ & [A_{Load}] [\Delta X_L] + [B_{Load}] [\Delta R_L] \end{aligned} \quad (47)$$

where $[A_{Loadinv}]_i = [A_{Ld1i} \ A_{Ld2i} \ A_{Ld3i}]$. The expanded forms of the matrices in the above equations are not shown for brevity.

E. Overall System

The small-signal model for the entire system can be obtained by combining the linearized equations of the various subsystems. For the considered two-converter system, and assuming that GFMI-1 is in the common reference frame, state equation shown in (48) are obtained. This approach can be easily extended to any number of parallel-connected GFMI.

$$\dot{[\Delta X]} = [A] [\Delta X] + [B] [\Delta U] \quad (48)$$

where

$$\begin{aligned} [\Delta X] &= [[\Delta X_{\text{inv}}]_1 [\Delta X_{\text{inv}}]_2 [\Delta X_L]]^T \\ [\Delta U] &= [[\Delta U_{\text{inv}}]_1 [\Delta U_{\text{inv}}]_2 [\Delta R_L]]^T \\ [A] &= \begin{bmatrix} [A_{\text{inv}}]_1 & [A_{\text{inv}}]_{1-2} & [A_{\text{invLoad}}]_1 \\ [A_{\text{inv}}]_{2-1} & [A_{\text{inv}}]_2 & [A_{\text{invLoad}}]_2 \\ [A_{\text{Loadinv}}]_1 & [A_{\text{Loadinv}}]_2 & [A_{\text{Load}}] \end{bmatrix} \\ [B] &= \begin{bmatrix} [B_{\text{inv}}]_1 & [0] & [0] \\ [0] & [B_{\text{inv}}]_2 & [0] \\ [0] & [0] & [B_{\text{Load}}] \end{bmatrix} \end{aligned}$$

III. SMALL-SIGNAL ANALYSIS

A small-signal model is developed for the test system given in Fig. 1, using the parameters given in Table I-II. The required operating point data are taken from a separate detailed simulation. This section validates the developed small-signal model against a detailed EMT model in PSCAD/EMTDC. A number of control and network parameters are selected following the eigenvalue analysis and are perturbed to identify their impact on inverter interactions.

A. Model Validation

To validate the developed small-signal model, its response is compared with that of a fully-detailed EMT model of the system in PSCAD/EMTDC. Fig. 8 compares the traces obtained from the two models for three types of disturbances, namely, a 0.1 pu decrement of R_L , 0.1 pu of impulse to $P_{\text{ref}1}$ for 0.1 s, 0.1 pu increment of E_{ref} of both the GFMI. These tests and others (not shown for brevity) verify that the developed small-signal model tracks the low-frequency contents of the response of the EMT model for adequately small disturbances around an operating point.

B. Eigen-Value Analysis

The eigenvalues of $[A]$ are obtained to identify the critical modes in the system. A complex conjugate pair at $-0.11 \pm 11.35j$ shows a mode with a damping ratio of 0.94% and an oscillation frequency of 1.8 Hz; it is identified as critical due to its low damping. Participation factors are calculated, which reveal that the following states have significant participation in the critical mode: δ_2 (100%), ω_1 (45%), ω_2 (45%), $i_{\text{cvd}1}$ (41%), $i_{\text{cvd}2}$ (41%), $i_{\text{cvdhp}1}$ (40%), $i_{\text{cvdhp}2}$ (40%). In calculating the participation factors, the magnitude of each participation factor is per unitized using the magnitude of the highest participating factor as the base quantity.

The dominant states are chiefly associated with the P - f controller and the transient VI paths. The inertia time

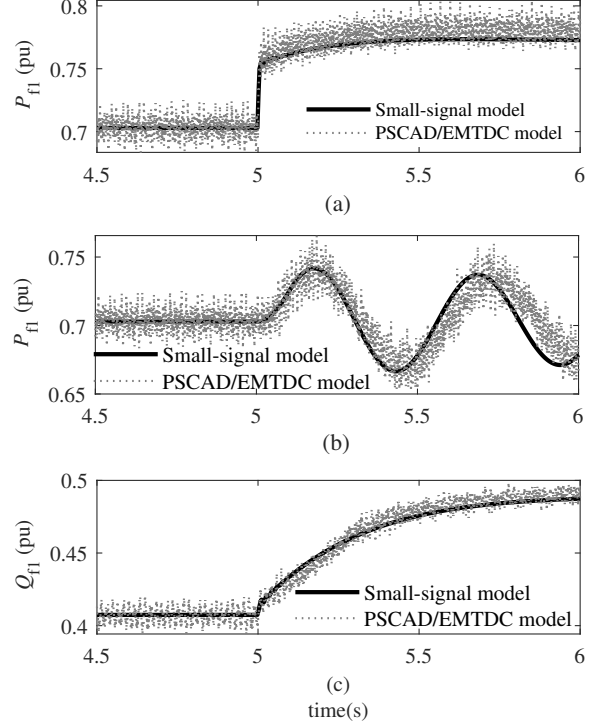


Fig. 8. Small signal model validation vs. EMT results (a) $\Delta R_L = -0.1$ pu, (b) $\Delta P_{\text{ref}1} = 0.1$ pu for 0.1 s (c) $\Delta E_{\text{ref}1} = \Delta E_{\text{ref}2} = 0.1$ pu, at $t = 5$ s.

constant (H) and droop co-efficient (D_p) mainly govern the dynamics of the P - f controller, while the dynamics of the transient VI are determined by the gain ($R_{\text{vi}0}$) and the cut-off frequency (f_{hp}). These control parameters are changed to assess their impact on the critical mode. Other than the controller states, converter currents' d-components have significant participation. Therefore, the LC filter's inductance is changed to evaluate its impact. The results obtained for the above parameter changes are presented in the following sections.

C. Impact of Inertia Time Constant (H)

The inertia time constant of GFMI-2 is set to 3 s and the inertia time constant of GFMI-1 is varied from 0.1 s to 5 s. The locus of the eigenvalues corresponding to the critical mode is given in Fig. 9, which shows that at least one GFMI with fast-acting capability (i.e., with a small inertia time constant) damps the oscillations quickly. When the inertia time constants of both inverters are large and in close vicinity, there is a higher likelihood of interactions and reaching instability.

Although the increment of inertia constant moves the system towards instability, the stable region of H values can be slightly extended by increasing the time constant of the Q - v droop, as shown in Fig. 10. This is because the increment of inertia time constant increases the response time of the P - f controller, which is given by $2HD_p$. Therefore, slowing down the PI controller in the Q - v path to match the dynamics of the slowed down P - f controller reduces the likelihood of

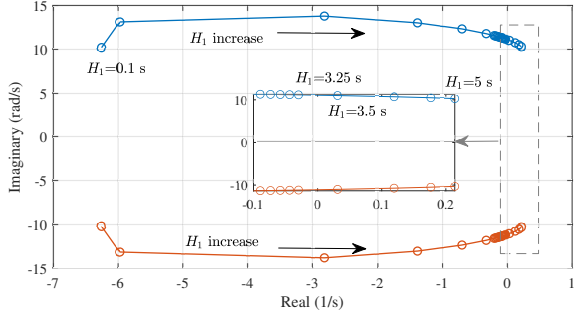


Fig. 9. Locus of the critical eigenvalues for changes in H_1 .

reaching instability. Note that this slows down the entire GFMI operation and diminishes their fast-acting abilities.

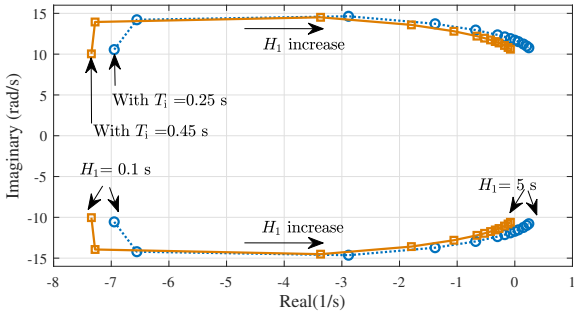


Fig. 10. Locus of the critical eigenvalues for changes in H_1 . Blue trace: $T_1 = 0.25$ s, Orange trace: $T_1 = 0.45$ s.

Even with identical control and network parameters, this low-damping mode exists, although it is not visible with a load disturbance as identical inverters share the load equally. This low-damping critical mode can be excited through a different disturbance, for example ΔP_{ref} of one of the machines. Fig. 11 compares each identical GFMI's virtual rotor oscillation obtained from PSCAD/EMTDC for a 0.1 pu reduction of R_L (Fig. 11 (a)) and for a ΔP_{ref} increment of 0.1 pu for 0.1 s in the GFMI-1 (Fig. 11 (b)). As expected for the load disturbance the parallel connected GFMI's respond identically and have no observable interactions. However, with the P_{ref1} impulse two GFMI's start to oscillate against each other. This shows the credibility of the small-signal modeling, which is carried out in the frequency domain in predicting the system oscillation modes as EMT results depend on the disturbance type.

In this study, though the network dynamics were modeled using dynamic phasors to reveal high-frequency interactions, the tested conditions result in an oscillatory mode of 1.8 Hz, which is in the electromechanical oscillation range. However, as shown in Fig. 12 depending on the GFMI control parameters the frequency of interactions can be high such that it requires the network to be modeled using dynamic phasors. To obtain these fast-acting GFMI's, each GFMI's H has been reduced from 3 s to 0.5 s and the integral time constant (T_i) has been reduced from 0.25 S to 0.01 s. This has resulted in an interaction frequency of 5.6 Hz, which certainly requires dynamic phasor modeling.

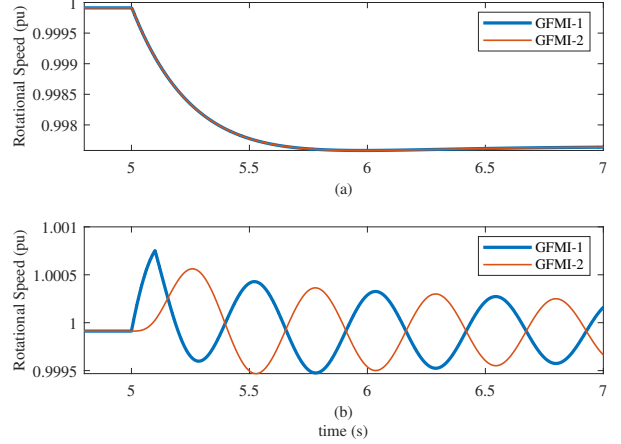


Fig. 11. Virtual rotor oscillation following (a) $\Delta R_L = -0.1$ pu and $\Delta P_{ref1} = 0.1$ pu for 0.1 s.

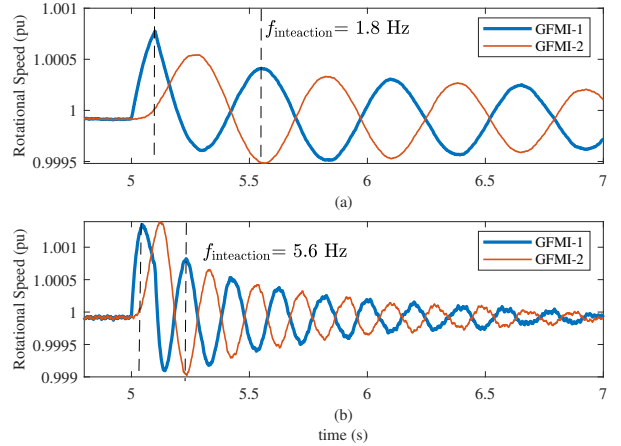


Fig. 12. Virtual rotor oscillation for $\Delta P_{ref1} = 0.1$ pu for 0.1 s (a) $H_1 = H_2 = 3$ s, $T_{i1} = T_{i2} = 0.25$ s, (b) $H_1 = H_2 = 0.5$ s, $T_{i1} = T_{i2} = 0.01$ s

D. Impact of Droop Coefficient (D_p)

The effect of D_p on the critical mode is evaluated by changing D_p of both GFMI's from 0.01 pu to 0.06 pu; Fig. 13 shows the shift of the critical eigenvalues, which confirms that large D_p values cause the system to reach instability. This is expected as large D_p values reduce the GFMI's power injections for a given frequency shift, therefore, raising the chance of oscillations following a disturbance.

E. Impact of the Transient VI Path

To evaluate the ability of the transient VI path to damp the critical mode, R_{vi0} is changed from 0.05 pu to 10 pu and f_{hp} is varied from 0.1 Hz to 10 Hz. As shown in Fig. 14 significant contribution from the transient VI path (i.e., with large R_{vi0} and small f_{hp} (in a certain range)) makes the system unstable. Therefore, it is concluded that the active damping path introduced through the transient VI path does not provide acceptable damping characteristics to the test system.

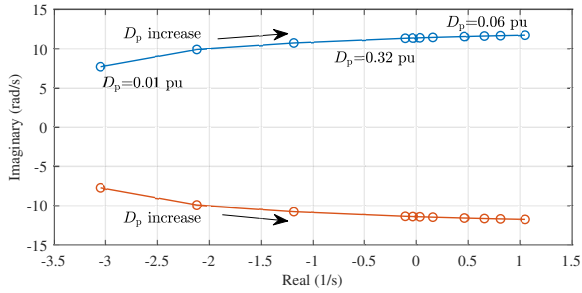


Fig. 13. Locus of the critical eigenvalues for changes in D_p for both inverters.

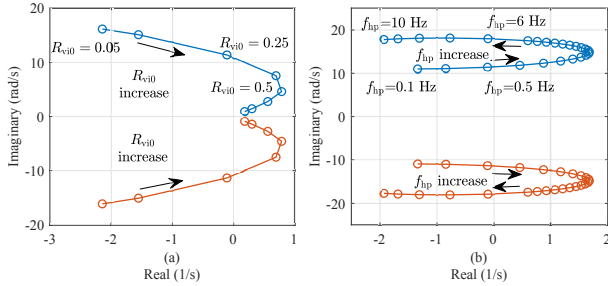


Fig. 14. Locus of the critical eigenvalues for changes in (a) $R_{v_{i0}}$ and (b) f_{hp} for both inverters.

F. Impact of LC Filter Inductance (L_f)

Due to the substantial participation of the d-components of the converter current in the critical mode, the LC filter inductances of both GFMI's are changed from 0.06 pu to 0.11 pu. The upper and lower limits of L_f are selected to avoid unnecessary voltage drops across the filter inductance and large THD levels in the converter current, respectively. Fig. 15 shows the trajectory of the critical eigenvalues following the increase of filter inductance. The tendency to reach instability is increased with lower filter inductance values. Oscillation frequency and damping ratio of the critical mode change negligibly with L_f .

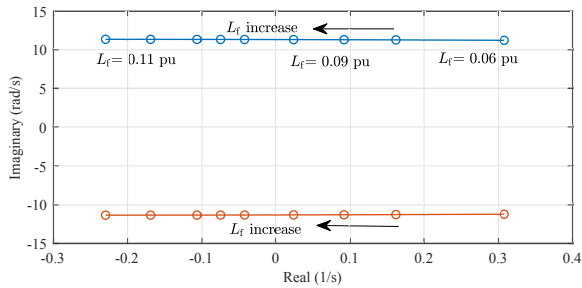


Fig. 15. Locus of the critical eigenvalues for changes in L_f in both inverters.

IV. CONCLUSIONS

The paper developed a small-signal model for a system of parallel-connected grid-forming inverters. The model is able to capture the low-frequency dynamic behavior of such systems. Eigenvalue analysis showed a critical interaction

frequency in the electro-mechanical frequency range. This low-frequency interaction is due to the low bandwidth of the tested grid-forming controller. However, grid-forming controllers with wide bandwidth can lead to high-frequency interactions requiring network dynamics to be modeled using dynamic phasors. The eigenvalue analysis further showed the impact of GFMI's controller and network parameters on the critical mode of the system. It was shown that large inertial constant (H) and droop co-efficient (D_p) values push parallel-connected GFMI's to oscillate against each other. Maintaining matching dynamics between the P - f controller and the Q - v controller paths shows to improve the stable region of operation without adding additional damping paths. Active damping introduced to the converter current through the transient VI path is not capable of providing improved damping characteristics to the system. The filter inductance can be selected to avoid undesired interactions between GFMI's. Even GFMI's with identical control and network parameters can oscillate against each other, although for some disturbance types these oscillations may not be visible. The study quantified the role of control and network parameters on a parallel-connected GFMI interactions.

REFERENCES

- [1] H. Alrajhi Alsiraji and R. El-Shatshat, "Comprehensive assessment of virtual synchronous machine based voltage source converter controllers," *IET Generation, Transmission & Distribution*, vol. 11, no. 7, pp. 1762–1769.
- [2] D. B. Rathnayake, M. Akrami, C. Phurailatpam, S. P. Me, S. Hadavi, G. Jayasinghe, S. Zabihi, and B. Bahrani, "Grid forming inverter modeling, control, and applications," *IEEE Access*, vol. 9, pp. 114 781–114 807, 2021.
- [3] A. D. Paquette and D. M. Divan, "Virtual impedance current limiting for inverters in microgrids with synchronous generators," *IEEE Trans. on Ind. Applicat.*, vol. 51, no. 2, pp. 1630–1638.
- [4] S. D'Arco, J. A. Suul, and O. B. Fosso, "A virtual synchronous machine implementation for distributed control of power converters in SmartGrids," *Electric Power Systems Research*, vol. 122, pp. 180–197.
- [5] Z. Shuai, W. Huang, Z. J. Shen, A. Luo, and Z. Tian, "Active power oscillation and suppression techniques between two parallel synchronverters during load fluctuations," *IEEE Trans. Power Electron.*, vol. 35, no. 4, pp. 4127–4142.
- [6] J. Liu, Y. Miura, H. Bevrani, and T. Ise, "Enhanced virtual synchronous generator control for parallel inverters in microgrids," *IEEE Trans. Smart Grid*, vol. 8, no. 5, pp. 2268–2277.
- [7] R. Rosso, S. Engelken, and M. Liserre, "Analysis of the behavior of synchronverters operating in parallel by means of component connection method (CCM)," in *2018 IEEE Energy Conversion Congress and Exposition (ECCE)*. IEEE, pp. 2228–2235.
- [8] X. Wang, F. Blaabjerg, and W. Wu, "Modeling and analysis of harmonic stability in an AC power-electronics-based power system," *IEEE Trans. Power Electron.*, vol. 29, no. 12, pp. 6421–6432.
- [9] P. Kundur, *Power System Stability and Control*. McGraw Hill, Inc.
- [10] N. Pogaku, M. Prodanovic, and T. C. Green, "Modeling, analysis and testing of autonomous operation of an inverter-based microgrid," *IEEE Trans. Power Electron.*, vol. 22, no. 2, pp. 613–625.
- [11] X. Wang and F. Blaabjerg, "Harmonic stability in power electronic-based power systems: Concept, modeling, and analysis," *IEEE Transactions on Smart Grid*, vol. 10, no. 3, pp. 2858–2870, 2018.